PAPER

Embedded atom method potential for studying mechanical properties of binary Cu–Au alloys

To cite this article: Adrien Gola and Lars Pastewka 2018 *Modelling Simul. Mater. Sci. Eng.* **26** 055006

View the article online for updates and enhancements.

Embedded atom method potential for studying mechanical properties of binary Cu–Au alloys

Adrien Gola[1,2] **and Lars Pastewka**[1,2]

[1] Institute for Applied Materials, Karlsruhe Institute of Technology, Straße am Forum 4, D-76131 Karlsruhe, Germany
[2] Department of Microsystems Engineering, University of Freiburg, Georges-Köhler-Allee 103, D-79110 Freiburg, Germany

E-mail: lars.pastewka@imtek.uni-freiburg.de

CrossMark

Abstract

We present an embedded atom method (EAM) potential for the binary Cu–Au system. The unary phases are described by two well-tested unary EAM potentials for Cu and Au. We fitted the interaction between Cu and Au to experimental properties of the binary intermetallic phases Cu_3Au, $CuAu$ and $CuAu_3$. Particular attention has been paid to reproducing stacking fault energies in order to obtain a potential suitable for studying deformation in this binary system. The resulting energies, lattice constant, elastic properties and melting points are in good agreement with available experimental data. We use nested sampling to show that our potential reproduces the phase boundaries between intermetallic phases and the disordered face-centered cubic solid solution. We benchmark our potential against four popular Cu–Au EAM parameterizations and density-functional theory calculations.

Supplementary material for this article is available online

(Some figures may appear in colour only in the online journal)

1. Introduction

The 'embedded atom' method (EAM) [1–5] is a widespread model for interatomic interactions in metals. It is nowadays put to use in molecular dynamics and Monte-Carlo (MC)

simulations that seek to describe complex properties from mechanical response [6, 7] to phase-equilibria in alloys [8, 9].

The binary Cu–Au system has been studied in recent years because multilayered (phase separated) films of Cu–Au can be prepared experimentally [10–12], yet Cu–Au is miscible and forms stable intermetallic phases. The phase separated state is therefore an example of a material far from equilibrium that can be used to study alloying by mechanical action [13, 14] and the influence of microstructure on mechanical properties [15–17]. Cu and Au both crystallize in the face-centered cubic (fcc) structure. Their intermetallic phases are of mainly $L1_0$ and $L1_2$ structure [10].

Studying deformation processes in this binary system requires an interatomic potential that captures both mechanical and thermodynamic properties. The benchmark property for the mechanical performance of an embedded atom potential for fcc metals is the stacking fault energy (SFE) [18], since deformation in fcc metals is mainly carried by dislocations that often dissociate into two Shockley partials separated by a stacking fault. The splitting distance between these partials is determined by SFE and elastic constants [19].

Most of the binary Cu–Au EAM potentials found in the literature [8, 20–22] are fitted to describe thermodynamic properties and provide an approximate description of the Cu–Au binary phase diagram [23], but they do not describe the energies of planar defects in pure phases well, such as stable and unstable stacking fault energies or surface energies. The present work reports an interatomic potential for the binary Cu–Au system that describes stacking faults well while conserving a reasonable description of the Cu–Au phase diagram. For this goal, we use the established Cu potential by Mishin *et al* [24] and the Au potential by Grochola *et al* [25] for the unary phases and only fit the Cu–Au cross interaction. This is a pragmatic approach to arrive at a potential energy expression that can be used to study mechanical deformation in the Cu–Au system. We compare the properties of this potential to four potentials published in the literature: Ackland *et al* [22], Barrera *et al* [8], Zhou *et al* [21] and the universal EAM of Foiles *et al* [20].

2. Methods

2.1. Embedded atom method

In the EAM, the total energy of an atomic configuration is given by $E = \sum_i E_i$ with

$$E_i = F_{\sigma_i}(\rho_i) + \frac{1}{2} \sum_{j \neq i} \phi_{\sigma_i \sigma_j}(r_{ij}). \tag{1}$$

Here, Latin i, j denote atom indices and Greek σ_i, σ_j denote the species of atoms i and j, respectively. The symbol r_{ij} is the distance between two atoms, $r_{ij} = |\vec{r}_i - \vec{r}_j|$, where $\vec{r}_i$ denotes the position of atom i. The total energy then depends on the local density of atoms ρ_i through the 'embedding function' $F_{\sigma_i}(\rho_i)$. The heuristic rationale here is that the nucleus of atom i is embedded in a gas of nearly free electrons whose density depends on the density of atoms in the neighborhood of atom i, an argument which can be supported by quantum-mechanical considerations [1, 5, 26]. The density is computed from

$$\rho_i = \sum_{j \neq i} f_{\sigma_i | \sigma_j}(r_{ij}), \tag{2}$$

where $f_{\sigma_i | \sigma_j}(r_{ij})$ is some function that drops to zero as $r_{ij} \rightarrow r_c$. The function $f_{\sigma_i | \sigma_j}(r_{ij})$ describes the contribution of an atom of species σ_j to the local density of an atom of species σ_i. Here, r_c is the range or cutoff radius of the embedded atom potential. The function $\phi_{\sigma_i \sigma_j}(r)$ in

Table 1. Lattice constant a_0 of the Cu and Au unary fcc phases from experiments (extrapolated to 0 K unless otherwise noted), density-functional theory (DFT) and the respective EAM potential (both at 0 K).

Element	Method	a_0 (Å)
Cu	Experimental [31]	3.615[a]
	DFT-PW91 [32]	3.637
	DFT-PBE (this work)	3.637
	Mishin *et al*	3.615
	Ackland *et al*	3.615
	Barrera *et al*	3.615
	Foiles *et al*	3.615
	Zhou *et al*	3.615
Au	Experimental [31]	4.07
	DFT-LDA[b] [33]	4.067
	DFT-PBE [33]	4.175
	DFT-PBE (this work)	4.157
	Grochola *et al*	4.070
	Ackland *et al*	4.078
	Barrera *et al*	4.079
	Foiles *et al*	4.080
	Zhou *et al*	4.080

[a] At 300 K.
[b] Local density approximation (LDA).

equation (1) is a pair-potential and symmetric with respect to exchange of the species σ_i and σ_j. The function $f_{\sigma_i|\sigma_j}(r)$ does not necessarily share this symmetry.

Most formulations of the EAM use an expression like equation (1). The major difference between different formulations is how the atomic species enter equations (1) and (2). For example, the widely used formulation of Daw and Baskes [3] uses $f_{\sigma_i|\sigma_j}(r_{ij}) = f_{\sigma_j}(r)$, i.e. the contribution of atom j to the density of atom i depends only on the type σ_j on atom j and not on the type σ_i of atom i. The formulation given in equations (1) and (2) is due to Finnis and Sinclair [2]. We employ this latter formulation here since it gives most flexibility. For the specific case of the binary Cu–Au system, we need to fit three functions, $f_{Cu|Au}(r)$, $f_{Au|Cu}(r)$ and $\phi_{AuCu}(r)$, for the cross potential.

For the pure phases we use the potential energy expressions given by Mishin *et al* [24] for Cu and Grochola *et al* [25] for Au. Both potentials report the three functions $F(\rho)$, $f(r)$ and $\phi(r)$ in a tabulated form [27]. Values and derivatives are then computed from a third-order spline approximation to this table. Mishin's potential has been fit to experimental and *ab initio* properties of Cu (lattice constant, heats of formation, etc) while Grochola has adopted the force-matching approach of Ercolessi and Adams [28] to fit the potential to *ab initio* (density-functional theory [29] with the PW91 functional [30]) data. While these fitting procedures differ in philosophy, both potentials give accurate representations of the underlying material. Tables 1–3 show a comparison of computed lattice parameters, elastic constants and planar defects in comparison with experimental and *ab initio* data for the unary phases as described by these potentials.

Table 2. Cubic elastic constants C_{11}, C_{12} and C_{44} and bulk modulus B of the unary fcc phases from experiments (at 0 K) and the respective EAM potential (at 0 K). Elastic constants were obtained from a finite-differences approximation of the derivative of the stress tensor using a strain increment of 10^{-6}. All results are given in GPa.

Element	Method	$C11$	$C12$	$C44$	B
Cu	Experimental [34]	176	125	82	142
	DFT-PW91 [32]	177	130	82	145
	DFT-PBE (this work)	179	126	78	143
	Mishin *et al*	170	122	76	138
	Ackland *et al*	169	122	76	137
	Barrera *et al*	163	117	75	132
	Foiles *et al*	167	124	76	139
	Zhou *et al*	178	128	78	145
Au	Experimental [34]	202	170	45	180
	DFT-LDA [33]	198	185	56	189
	DFT-PBE [33]	147	136	40	140
	DFT-PBE (this work)	155	130	26	138
	Grochola *et al*	202	169	46	180
	Ackland *et al*	187	157	42	167
	Barrera *et al*	186	148	49	161
	Foiles *et al*	183	159	45	167
	Zhou *et al*	188	158	43	168

2.2. Ab initio calculations

We computed reference values using DFT. These calculations were carried out using the Vienna *ab initio* Simulation Package (VASP version 5.3.2) [41–43]. We use the projector-augmented wave (PAW) [44] method to represent frozen core electrons and the Perdew–Burke–Ernzerhof (PBE) [45] exchange correlation functional. For both elements we used the standard potentials distributed with VASP with PAW electronic configuration [Ar] $3d^{10} 4p^1$ for Cu and [Xe] $4f^{14} 5d^{10} 6s^1$ for Au. All calculations were spin-paired. The wavefunctions were expanded into plane waves up to an upper energy cutoff of 500 eV. The Brillouin-zone was sampled with a $15 \times 15 \times 15$ k-points mesh distributed according to the sampling scheme of Monkhorst and Pack [46] for bulk properties (lattice constants, elastic constants, etc). We used an $11 \times 1 \times 11$ Monkhorst and Pack mesh for systems containing planar defects (stacking faults or surfaces). Energy level were populated using the method of Methfessel and Paxton [47] with a smearing width of 0.2 eV.

2.3. Stacking fault energies

The intrinsic stacking fault is a lattice defect that breaks the stacking sequence …ABCAB-CABC… of {111} planes in the fcc structure to …ABCABABC…. Atoms in the stacking fault are locally in a hexagonal close packed (hcp) environment. The energy for forming this defect is positive and called the SFE.

Stacking faults can be characterized by the γ-surface [48], the potential energy surface that is obtained by rigidly displacing a crystalline block of atoms parallel to a {111} plane. In the case of an fcc structure the local minima of the γ-surface in the $\langle 112 \rangle$ direction are stable stacking faults and the respective energy is the SFE. Saddle points are called unstable stacking faults. For the $L1_2$ structure the γ-surface is more complex. The local minima

Table 3. Energies of planar defects in the unary fcc phases. The table reports the intrinsic stacking fault energy γ_{SF}, the unstable stacking fault energy γ_{USF} and the energies of free {100}, {110} and {111} surfaces (γ_{100}, γ_{110} and γ_{111}, respectively). Values in parenthesis are computed without atomic relaxation. Values in curly brackets are corrected DFT values using the technique described in [35]. Experimental and previous *ab initio* calculation results are shown when available. All the results are in mJ m^{-2}. Large deviations between theoretical and experimental data are shown in bold and discussed in the main text.

Phase	Method	γ_{SF}	γ_{USF}	γ_{100}	γ_{110}	γ_{111}
Cu	Experimental	45–75[a]	—	1790[b]	1790[b]	1790[b]
	DFT (literature)	39[c]	158[c]	1460 (1470) {2270}[d]		1320 (1320) {2130}[d]
		43[e]	175[e]			
		49[f]	210[f]			
	DFT-PBE (This work)	51 (51)	161 (179)	1408 (1423) {2021}	1495 (1539) {2108}	1223 (1226) {1836}
	Mishin *et al*	44.4 (44.8)	162 (180)	1347 (1352)	1478 (1492)	1241 (1248)
	Ackland *et al*	46.4 (52.1)	**289 (297)**	1135 (1144)	1230 (1253)	**960 (969)**
	Barrera *et al*	**17.8 (17.8)**	154 (159)	1331 (1354)	1446 (1473)	1225 (1254)
	Foiles *et al*	**17.4 (17.8)**	141 (157)	1288 (1291)	1413 (1427)	1181 (1185)
	Zhou *et al*	22.6 (39.8)	110 (179)	1563 (1566)	1744 (1756)	1502 (1505)
Au	Experimental	32–40[a]	—	1506[b]	1506[b]	1506[b]
	DFT (literature)	27[e]	94[e]	1450[d]		1250[d]
	DFT-PBE (This work)	36 (39)	87 (103)	835 (840) {1261}	883 (894) {1309}	646 (648) {1072}
	Grochola *et al*	42.6 (42.7)	92 (98)	1296 (1439)	1530 (1735)	1196 (1281)
	Ackland *et al*	31.7 (44.3)	**219 (296)**	**769 (794)**	**814 (871)**	**622 (644)**
	Barrera *et al*	**−1.5 (−1.3)**	117 (136)	**683 (766)**	**738 (851)**	**577 (645)**
	Foiles *et al*	**4.8 (4.8)**	95 (103)	914 (976)	977 (1094)	785 (827)
	Zhou *et al*	**3.3 (5.1)**	86 (106)	1015 (1083)	1109 (1236)	907 (952)

[a] Reference [36].
[b] Reference [37], extrapolated to 0 K for average orientation.
[c] PW91 [38].
[d] PW91 [39].
[e] PBE [40].
[f] LDA [18].

correspond successively to the complex stacking fault (CSF) energy (at $\frac{a_0}{6}[11\bar{2}]$), the anti-phase boundary energy (at $\frac{a_0}{2}[11\bar{2}]$) and the superlattice intrinsic stacking fault (SISF) energy (at $\frac{2a_0}{3}[11\bar{2}]$) [49]. For the $L1_0$ structure one can find the SISF energy at $\frac{a_0}{6}[11\bar{2}]$ and the CSF at $\frac{a_0}{12}[\bar{1}\bar{1}2] + \frac{a_0}{4}[1\bar{1}0]$ [50]. In an atomistic calculation, the SFE γ_{SF} can be computed from

$$\gamma_{SF} = \frac{E_{SF} - E_0}{A}, \tag{3}$$

where E_{SF} is the energy of the crystal with defect (hcp stacking fault in our case), E_0 is the energy of the perfect lattice, and A is the area of the stacking fault.

All stacking fault energies reported here were computed at 0 K. We used systems composed of 12 atomic layers with two free surfaces separated by a 15 Å vacuum. The x, y and z axis of the simulation box were oriented along the [112], [$\bar{1}$10] and [$\bar{1}\bar{1}$1] directions, respectively. We then displaced the upper six atomic layers rigidly in the [112] direction while computing the energy.

In order to quantify the effect of lattice relaxation, we carried out additional calculations where we allowed relaxation of atoms along the [$\bar{1}\bar{1}$1] direction. These calculations were run for only the EAM potentials and used larger crystalline blocks of approximately 48 000 atoms originally in perfect fcc stacking. We used a conjugate gradient minimizer and optimized until the length of the global force vector of the system dropped below 10^{-6} eV Å^{-1}.

2.4. Surface energies

The surface energy is the energy of another planar defect, the interface of the crystal with vacuum. Its energy represents the work required to create a free surface from a perfect fcc bulk on a given (hkl) plane. Similarly to the stacking fault definition, surface energies can be computed from

$$\gamma_{hkl} = \frac{E_{hkl} - E_0}{2A}, \tag{4}$$

where E_{hkl} is the energy of the crystal with two free surfaces, E_0 is the energy of the perfect lattice (fcc in our case), and A is the area of the two planar faults created.

All surface energies reported here are computer at 0 K. We computed the surface energies for three low-index crystallographic planes {100}, {110} and {111}. In *ab initio* calculations we used systems similar to the one used for the SFE calculations. The systems were set up such that at least 30 Å separated the two free surfaces. We used a stack of 8 crystalline layers for the (100) orientation, 12 layers for the (110) orientation and 9 layers for the (111) orientation. Free surfaces were relaxed using a conjugate gradient minimizer until the length of the global force vector of the system dropped below 10^{-3} eV Å^{-1}.

The energies of (free) surfaces computed from DFT calculations using the both LDA or GGA approximations typically underestimate the corresponding experimental values. We here applied the correction by Mattsson *et al* [35] to our DFT surface energy results. This correction uses the intrinsic error of the corresponding functional (PBE in our case) as computed for the Jellium surface (for which high-quality random phase approximation data is available [51, 52]) to correct the surface energy of DFT calculations.

2.5. Nested sampling

We used nested sampling [53–57] to compute the temperature/composition phase diagram of the binary Cu–Au system. In brief, nested sampling directly constructs the phase space

volume $\chi(\varepsilon)$ as a function of potential energy ε. Assume we have some initial energy ε_l, and K random phase space configurations uniformly distributed within the phase space volume bounded by ε_l. Let E_i denote the (potential) energy of the ith configuration, ordered in order of decreasing energy with maximum energy $E_1 \equiv \varepsilon_l$. Since all E_i cover phase space (up to ε_l) uniformly, discarding the configuration with the highest energy E_1 leads to $K - 1$ remaining configurations that cover a phase space volume approximately $K/(K + 1)$ smaller than the initial one and bounded by energy $\varepsilon_{l+1} \equiv E_2$. An additional configuration is then added to the $K - 1$ configurations by cloning a random previous configuration and propagating it using a combination of molecular dynamics [58] and Markov chain MC steps. This generates a series of decreasing energy values ε_l with corresponding phase space volumes $\chi(\varepsilon_l) = \chi(\varepsilon_1)[(K - 1)/K]^{(l-1)}$, which constitutes a discretization of $\chi(\varepsilon)$.

Our calculations used unit cells containing 64 atoms. We used $K = 2400$ phase space configurations and stopped the nested sampling algorithm when the expectation value of the temperature dropped below 100 K. We removed one configuration per iteration and generated the new uncorrelated configuration with a MC walk of 640 MC moves. The MC walk was a repeating sequence of eight N-particle moves, 16 cell volume moves, eight MC cell shear moves, eight cell stretch moves and eight atom swaps. We then used $\chi(\varepsilon)$ to compute the heat capacity $C_p(T)$ as a function of temperature T. Peaks within $C_p(T)$ indicate phase transitions. We fitted these peaks with Gaussians. This yields the transition temperatures and a measure for their error.

3. Fitting the cross potential

We used the two unary EAM potentials of Mishin and Grochola as the starting point for our binary Cu–Au EAM potential. We adopted a simplified procedure for determining the cross term, inspired by the (Lorentz–Berthelot) type mixing rules that are commonly used for cross terms in Lennard-Jones type potentials, but also the embedded atom method (e.g. Foiles *et al* [59]) or empirical bond-order potentials (e.g. Tersoff *et al* [60]). Rather than employing a simple mix that treats the contribution of both species equally (either through arithmetic or geometric averages), we fitted (scalar) mixing parameters. This leads to small set of fitting parameters while still giving some flexibility for the target properties to be reproduced.

Specifically, we used the expression

$$\phi_{\mathrm{CuAu}}(r) = \alpha_{\mathrm{Cu}} \cdot \phi_{\mathrm{CuCu}}(r) + \alpha_{\mathrm{Au}} \cdot \phi_{\mathrm{AuAu}}(r) \tag{5}$$

for the repulsive pair-potential in equation (1). Here, $\phi_{\mathrm{CuAu}}(r)$ is the pairwise interspecies potential and $\phi_{\mathrm{CuCu}}(r)$ and $\phi_{\mathrm{AuAu}}(r)$ are the pairwise potentials for the pure species (i.e. Mishin's and Grochola's estimates for those). The coefficients α_{Cu} and α_{Au} are the mixing parameters and fit using the procedure described below. Note that equation (5) conserves the symmetry of $\phi_{\sigma_i \sigma_j}(r)$ with respect to exchange of the indices σ_i and σ_j.

The local electron densities were obtained from the functions

$$f_{\mathrm{Au}|\mathrm{Cu}}(r) = \beta_{\mathrm{Cu}} \cdot f_{\mathrm{Cu}|\mathrm{Cu}}(r) + \gamma_{\mathrm{Cu}} \cdot f_{\mathrm{Au}|\mathrm{Au}}(r), \tag{6}$$

$$f_{\mathrm{Cu}|\mathrm{Au}}(r) = \beta_{\mathrm{Au}} \cdot f_{\mathrm{Au}|\mathrm{Au}}(r) + \gamma_{\mathrm{Au}} \cdot f_{\mathrm{Cu}|\mathrm{Cu}}(r), \tag{7}$$

where $f_{\mathrm{Au}|\mathrm{Cu}}(r)$ and $f_{\mathrm{Cu}|\mathrm{Au}}(r)$ are the missing cross terms.

The coefficients in equations (5)–(7) were fitted to experimental data for each of the intermetallics. The (experimental) target properties for the Cu_3Au, $CuAu$ and $CuAu_3$ phases are marked with a dagger in tables 4 and 5.

Table 4. Lattice constant a_0 for the cubic $L1_2$ phases, lattice constants a_0 and c_0 for the tetragonal $L1_0$ phase and enthalpy of mixing ΔH_{mix} of the Cu–Au binary phases from experiments at 0 K, DFT and the respective EAM potential (at 0 K). Large deviations between theoretical and experimental data are shown in bold and discussed in the main text. The values marked with a dagger are fitting targets for the potential. The error relative to the experimental enthalpy of mixing at 0 K is given in percent in the last column.

Phase	Method	a_0 (Å)	c_0 (Å)	c/a	ΔH_{mix} (eV/atom)	Error (%)
Cu$_3$Au ($L1_2$)	Experimental	3.74† [31]			−0.074† [62]	—
	DFT (literature)	3.725[a] [33]			—	—
	DFT-PBE (this work)	3.784			−0.048	35
	EAM (this work)	3.735			−0.072	3
	Ackland *et al*	3.748			−0.071	4
	Barrera *et al*	3.726			−0.081	9
	Foiles *et al*	3.753			−0.051	31
	Zhou *et al*	3.750			−0.093	26
CuAu ($L1_0$)	Experimental	3.966†[b] [8]	3.673†[b]	0.93†	−0.091†[62]	—
	DFT-PBE (this work)	4.061	3.679	0.91	−0.058	36
	EAM (this work)	3.852	3.803	0.99	−0.092	1
	Ackland *et al*	3.899	3.902	**1.00**	−0.071	22
	Barrera *et al*	3.944	3.653	0.93	−0.094	3
	Foiles *et al*	3.070 (**B2**)	—	—	−0.082	10
	Zhou *et al*	3.941	3.715	0.94	−0.133	46
CuAu$_3$ ($L1_2$)	Experimental	3.98†[b] [31]			−0.059†[62]	—
	DFT-PBE (this work)	4.047			−0.028	53
	EAM (this work)	3.941			−0.060	2
	Ackland *et al*	3.997			−0.057	3
	Barrera *et al*	3.960			−0.052	12
	Foiles *et al*	3.982			−0.035	41
	Zhou *et al*	3.976			−0.095	61

[a] Calculated with the revised PBE functional of [71].
[b] At 300 K.

We fitted the cross potential by minimizing a cost function Q with respect to the model parameters using the downhill simplex method of Nelder and Mead [61]. The cost function was a sum of the weighted residuals for each targeted physical constant,

$$Q = \sum_i (\delta_i \cdot w_i)^2, \qquad \delta_i = v_{i,\text{EAM}} - v_{i,0}, \tag{8}$$

where i is the ith physical constant value to fit, $v_{i,\text{EAM}}$ and $v_{i,0}$ are the computed and targeted physical constants, respectively, and w_i is a weighting coefficient. The initial values entering equations (5)–(7) were taken as $\alpha_{\text{Cu}} = \alpha_{\text{Au}} = \beta_{\text{Cu}} = \beta_{\text{Au}} = \gamma_{\text{Au}} = \gamma_{\text{Cu}} = 0.5$ with the weight coefficients defined in table 6. The lattice constant of the $L1_2$ phase did not require a high weight as the value from the initial guess already agreed well with experimental data. For the $L1_0$ a high weight was required to obtain the correct c/a ratio. We put a particular focus on

Table 5. Independent elastic constants and bulk modulus B of the $L1_2$ and $L1_0$ phases from experiments (at 0 K) and the respective EAM potential (at 0 K). Elastic constants were obtained from a finite-differences approximation of the derivative of the stress tensor using a strain increment of 10^{-6}. All results are given in GPa. The values marked with a dagger are fitting targets for the potential. The averaged error relative to the experimental value over all the elastic constant is given in percent in the last column.

Element	Method	C_{11}	C_{12}	C_{44}	B	Averaged error (%)
Cu$_3$Au ($L1_2$)	Experimental [34]	189†	132†	74†	150	—
	DFT [33]	198	154	91	169	13
	DFT-PBE (this work)	178	120	65	139	9
	EAM (this work)	236	172	78	194	22
	Ackland *et al*	177	126	65	143	7
	Barrera *et al*	174	124	66	140	8
	Foiles *et al*	175	140	60	151	8
	Zhou *et al*	124	107	47	112	29
CuAu$_3$ ($L1_2$)	Experimental [34]	189†	155†	47†	166	—
	DFT-PBE (this work)	157	123	36	134	20
	EAM (this work)	220	193	50	202	17
	Ackland *et al*	269	192	96	218	50
	Barrera *et al*	194	149	57	164	7
	Foiles *et al*	181	155	47	164	1
	Zhou *et al*	192	150	55	164	6

Element	Method	C_{11}	C_{22}	C_{12}	C_{13}	C_{44}	C_{55}
CuAu ($L1_0$)	DFT-PBE (this work)	264	269	157	272	189	37
	EAM (this work)	228	250	176	186	71	70
	Ackland *et al*	214	280	184	158	84	100
	Barrera *et al*	198	148	144	127	59	59
	Foiles *et al* (B2)	171	—	154	—	58	—
	Zhou *et al*	183	130	126	128	60	50

the enthalpy of mixing in order to conserve thermodynamic properties. The c/a ratio was constrained to be smaller than 1. An initial fit gave values for the prefactors γ_{Cu} and γ_{Au} smaller than 0.01. We then reran the fit at fixed $\gamma_{Cu} = 0$ and $\gamma_{Au} = 0$. This produced the final prefactors reported in table 7.

4. Tests of the binary potential

4.1. Lattice parameters and elastic constants

The physical properties (enthalpy of mixing, lattice constants, elastic constants) obtained for the ordered phases in our potential are shown in tables 4 and 5. The enthalpies of mixing are in good agreement with the experimental values with differences of less than 2 meV for the $L1_2$ phases. The lattice constants for the $L1_2$ phases are within a 1% range from the experimental values. The potential predicts a slightly deformed version of the tetrahedral $L1_0$ phase with a 2% smaller a_0 lattice vector and a 2% larger c_0 lattice vector, while keeping a c_0/a_0 ratio smaller than one (consistent with the $L1_0$ structure) and almost no error in density (differs by 0.2%). While structure and formation energy is excellently described by the EAM

Table 6. Weight coefficients used in equation (8) to fit to the experimental target data tabulated in tables 4 and 5. Fitting targets marked with a dagger in tables 4 and 5.

Phase Structure	Cu_3Au $L1_2$	CuAu $L1_0$	$CuAu_3$ $L1_2$
a_0	1	20	1
c_0		40	
c/a		80	
ΔH_{mix}	30	30	30
C_{11}	10		10
C_{12}	10		10
C_{44}	10		10

Table 7. Optimized set of mixing parameters for the binary EAM potential.

	Au	Cu
α	0.397	0.857
β	0.699	1.124
γ	0	0

potential, the elastic constants (table 5) for the intermetallic $L1_2$ phases are overestimated by $\sim$17% ($CuAu_3$) and $\sim$22% (Cu_3Au).

Existing EAM potentials manage to describe properly the elastic constants for the Cu and Au pure phases. The potentials from Ackland *et al* [22], Barrera *et al* [8] and Foiles *et al* [20] successfully describe the elastic properties of the Cu_3Au $L1_2$ phase, while the potential from Zhou *et al* [21] slightly underestimates the elastic constants for this phase. The potential from Ackland *et al* [22] overestimates the elastic constants for the $CuAu_3$ $L1_2$ phase when the three other correctly describe the elastic constant for this phase.

4.2. Stacking fault energies

Figure 1 shows the energy of the fault as a function of the relative displacement of the two ideal crystals bounding the stacking fault. For the Cu, Au and CuAu single crystals, the intrinsic SFE (γ_{SF}) is defined as the first minimum of the curve. For the Cu_3Au and $CuAu_3$ curve the first minimum corresponds to the complex SFE (γ_{CSF}). The unstable SFE to nucleate the leading partial can be identified as the first maximum of the curve [66].

Table 3 reports experimental planar defect energies [36, 38] and values obtained for the unary Cu and Au EAMs of Mishin *et al* [24] and Grochola *et al* [25] as well as the binary Cu–Au EAM potentials of Ackland *et al* [22], Barrera *et al* [8], Zhou *et al* [21] and the universal EAM of Foiles *et al* [20] for the unary phases. Both Mishin *et al* and Grochola *et al*, and hence also the binary potential presented here, agree well with experimental and DFT data for stacking fault and unstable stacking fault energies. Except for Ackland *et al*, the binary Cu–Au potentials underestimate the SFE of Au by an order of magnitude and the SFE of Cu by at least a factor of two. Conversely, while all potentials give unstable SFEs that agree well with DFT, Ackland *et al* gives unstable stacking fault energies about a factor of two larger than the reference DFT calculations.
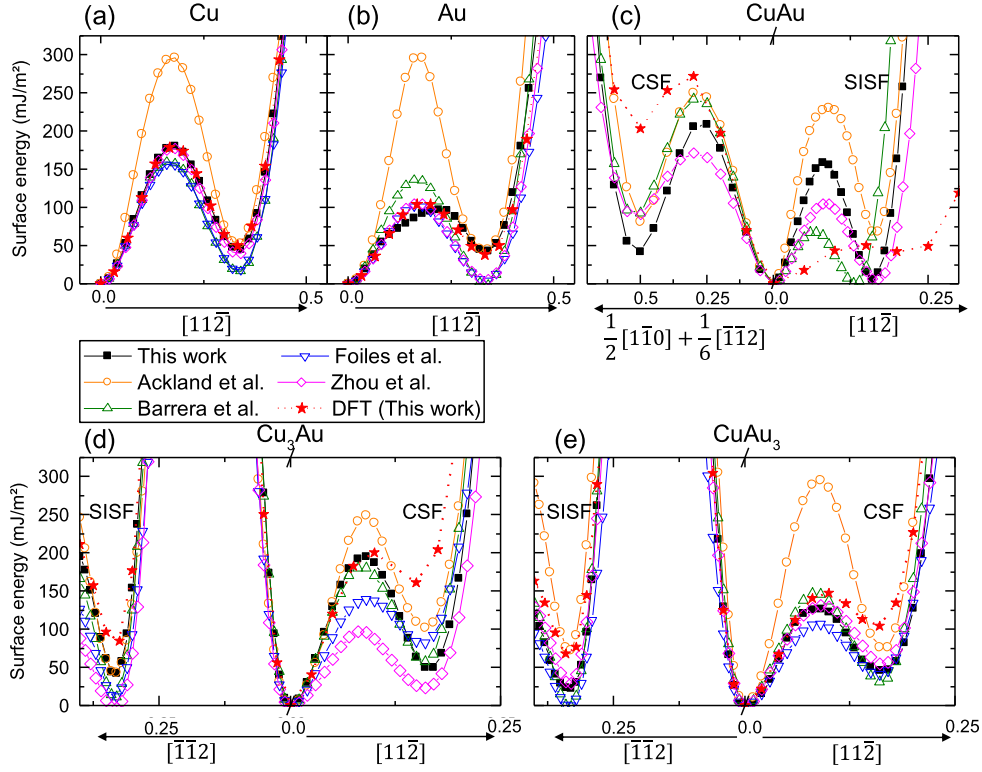
Figure 1. Generalized stacking fault energies of the single crystal Cu, Cu_3Au, CuAu, $CuAu_3$ and Au (without $\langle 111 \rangle$ axis relaxation for all calculations) for the potentials considered in this work and DFT calculations. The directions of the rigid displacements within the corresponding (111) plane are indicated in the axis labels.

We also compared the CSF and SISF energies obtained for the binary phases with DFT calculation. Results are summarized in table 8. All stacking fault values obtained for ordered phases with our potential are positive. The values for the $L1_2$ phases are underestimated by a factor of two to three. The values for the $L1_0$ phases are underestimated by a factor of six to seven. We note that both Ackland *et al* [22] and Zhou *et al* [21] yield reasonable values for the stacking faults of these three compounds (to within a factor of three of our DFT calculations). Barrera *et al* [8] and Foiles *et al* [20] give negative SISF energies for the $CuAu_3$ $L1_2$ structure. This indicates that $CuAu_3$ is not $L1_2$ in these potentials. Barrera *et al* [8] does additionally have a SISF energy for CuAu that is close to zero, also indicating a problem with the stability of the $L1_0$ CuAu phase in this potential.

4.3. Surface energies

The {100}, {110} and {111} surface energies are well described by all EAM potentials (tables 3 and 8) except for Barrera *et al* [8] that underestimates the values for Cu and Au by a factor of two or more and Ackland *et al* [22] that gives values for Au equal to half of the experimental or DFT values.

Table 8. Energies of planar defects in the binary phases. The table reports the complex stacking fault energy γ_{CSF}, the superlattice intrinsic stacking fault energy γ_{SISF} and the energies of free {100}, {110} and {111} surfaces (γ_{100}, γ_{110} and γ_{111}, respectively). Previous *ab initio* calculation results are shown when available. Values in parenthesis are computed without atomic relaxation. All the results are in mJ m^{-2}. Large deviations between theoretical and experimental data are shown in bold and discussed in the main text.

Phase	Method	γ_{CSF}	γ_{SISF}	γ_{100}	γ_{110}	γ_{111}
Cu$_3$Au ($L1_2$)	DFT	260[a] [63]	120[a] [63]			
		369[b] [64]	199[b] [64]			
		227[a] [65]				
	DFT-PBE (this work)	133 (161)	76.7 (79.4)	1274 (1294)	1301 (1385)	1074 (1086)
	EAM (this work)	17.6 (48.5)	20.4 (41.0)	1408 (1456)	1576 (1655)	1317 (1354)
	Ackland *et al*	48.8 (102.5)	40.6 (42.4)	1020 (1044)	1100 (1145)	864 (882)
	Barrera *et al*	47.3 (58.3)	10.9 (10.9)	1145 (1164)	1235 (1266)	1031 (1044)
	Foiles *et al*	58.2 (82.3)	11.2 (11.5)	1122 (1155)	1223 (1288)	997 (1028)
	Zhou *et al*	19.9 (24.0)	**−3.4 (−3.3)**	1475 (1484)	1626 (1669)	1372 (1385)
CuAu ($L1_0$)	DFT-PBE (this work)	167 (201)	35.9 (40.5)	1071 (1091)	1121 (1222)	906 (937)
	EAM (this work)	22.3 (40.5)	5.8 (6.3)	1445 (1512)	1592 (1680)	1311 (1383)
	Ackland *et al*	46.0 (80.8)	65.2 (65.5)	982 (1021)	976 (1060)	584 (775)
	Barrera *et al*	75.3 (89.2)	**0.6 (0.6)**	1014 (1041)	1038 (1098)	1398 (1600)
	Zhou *et al*	81.6 (88.8)	22.8 (22.9)	1384 (1408)	1483 (1552)	1235 (1263)
CuAu$_3$ ($L1_2$)	DFT	220[b] [64]	119[b] [64]			
	DFT-PBE (this work)	88.7 (104)	57.8 (65.6)	960 (986)	973 (1070)	774 (798)
	EAM (this work)	39.6 (46.1)	21.4 (21.9)	1360 (1454)	1564 (1727)	1263 (1328)
	Ackland *et al*	51.2 (73.8)	61.6 (71.9)	849 (885)	907 (970)	702 (731)
	Barrera *et al*	26.4 (30.9)	**−1.7 (−1.7)**	807 (854)	866 (941)	696 (729)
	Foiles *et al*	31.6 (41.0)	**−0.8 (−0.7)**	951 (1019)	1016 (1144)	816 (871)
	Zhou *et al*	50.5 (54.7)	27.6 (28.8)	1186 (1235)	1295 (1393)	1067 (1103)

[a] Full-potential linear muffin-tin orbital (LMTO) calculations using the local density approximation without relaxation.
[b] Tight-binding LMTO calculations without relaxation.

4.4. Binary phase diagram

We now explore the phase diagram of Cu–Au using the nested sampling method. We computed the heat capacity (at constant pressure) as a function of temperature, $C_P(T)$ for alloy compositions with $0, 25, 50, 75$ and 100 at% Cu. For the potential presented here we additionally consider $9, 34, 66$ and 91 at% Cu. A typical $C_P(T)$ curve derived from one of theses calculations is shown in the inset of figure 2. Each peak indicates a first order phase transition. The location of these individual peaks is reported along the experimental phase diagram shown in figure 2. We fitted a Gaussian to the peaks in the $C_P(T)$ curves to determine mean and error of the transition temperature. The error bars shown in figure 2 are the standard deviation of this Gaussian.

We computed the phase diagrams for the EAM potentials listed in table 3 as well as our potential. Compared to experimental values [67], our nested sampling calculations show that Grochola *et al* slightly underestimates the melting point of Au (by around 100 K) and Mishin *et al* overestimates the melting point of Cu (by around 100 K). There are only two potentials with a clear depression of the melting point at intermediate composition, Foiles *et al* [20] and Ackland *et al* [22]. Both, however underestimate the melting points of the binary phases by more than 150 K. (All other potentials are within 100 K of the experimental melting point.) The potential by Ackland *et al* [22] shows two phase transitions for the pure Au phase which should have just a transition from fcc to the melt. The first transition (at high temperature) corresponds to the transition from the liquid state to an ordered bcc-rich phase, the second point corresponds to a solid phase transition to a pure fcc structure.

Our potential shows a clear transition from solid solution to ordered intermetallic phases. These transitions from solid solution to ordered phases are described by almost all EAM potentials at temperatures about half the experimental values, except for the correct prediction of the transition temperature at 50 at% Cu by Foiles *et al* [20]. Only the potential by Ackland *et al* [22] severely overestimates the temperatures of the solid phase transitions of the $CuAu_3$ and CuAu phases.

We now inspect the structure of the low-temperature phases obtained from the nested sampling calculations for those structures that show negative stacking fault energies. Note that we have a total of $K = 2400$ ground state configurations for each composition. Automatic classification of binary lattice structures is difficult and we here report only on structures we manually inspected and analyzed with a combination of the adaptive common neighbor analysis [68, 69] and polyhedral template matching [70]. All ground state structures can be found in the supplementary material available online at http://dx.doi.org/10.6084/m9.figshare.6210413.

We find that Barrera *et al* [8] forms an hcp phase for pure Au at low temperatures, consistent with the negative SFE for fcc Au (see table 3) which indicates that the fcc phase is not the ground state. Similarly, CuAu $L1_0$ has a close to zero SISF energy in Barrera *et al* [8] and might therefore be metastable. The low-temperature intermetallic for this composition found by our nested sampling calculations gives an hcp-like structure and not $L1_0$. The negative SISF energies of the $CuAu_3$ ($L1_2$) phase in Barrera *et al* [8] and Foiles *et al* [20] are in agreement with our nested sampling ground state, where we obtain mixed hcp/fcc-like structures in both cases at low-temperature. For the potential of Foiles *et al* [20], the CuAu phase collapses into a B2 (bcc-like) structure when starting from an $L1_0$ structure during a cell shape and volume optimization. We confirm this ground state by inspecting our nested sampling calculations. The Cu_3Au ($L1_2$) phase in Zhou *et al* [21] has a negative superlattice
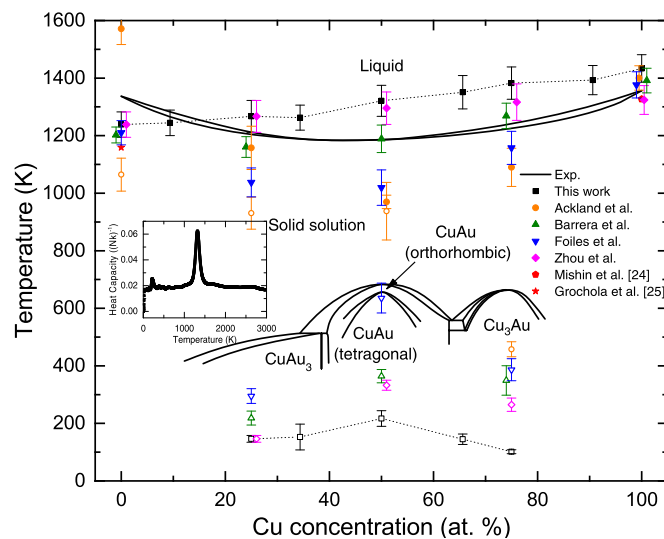
Figure 2. Phase diagram of the Cu–Au system. Solid lines are experimental data from [67]. Red data points show melting points reported in [24, 25]. All other results were computed using nested sampling. Full symbols represent liquid to solid transition, open symbols represent solid phase transitions. The dotted line connects data points and is a guide the eye. The inset exemplarily shows the nested sampling result of the heat capacity $C_p(T)$ for CuAu and the EAM potential of this work. Phase boundaries in the diagram are the positions of peaks of this curve. Overlapping points have been offset slightly in the concentration axis for clarity.

SISF energy. Consistent with this, our nested sampling calculations predict an hcp-like structure as the ground state at low-temperature.

5. Summary and conclusions

Capturing all the features of a complex system such as a binary alloy with a simple potential energy expression is a difficult task. There are numerous existing EAM parameterizations for the Cu–Au system in the literature, four of which [8, 20–22] we have explicitly tested here. Each of the potentials manages to describe a part of the properties spectrum. Ackland *et al* [22] gives good SFEs but does not describe the phase diagram well. The other three potentials [8, 20, 21] give a good reproduction of the phase diagram but underestimate SFEs. The most significant failure of all of the potentials tested here is that they do not describe the correct ground state for some of the binary phases.

The new potential presented here as a mix between the Cu potential of Mishin *et al* [24] and the Au potential of Grochola *et al* [25] gives a good description of both SFEs and the phase diagram. In particular, our potential gives reasonable energies for planar defects energies (stacking faults and surfaces), with the exception of the CuAu $L1_0$ phase where the SFE is underestimated by 85% with respect to DFT calculations. Its thermodynamic properties (enthalpy of mixing) for the binary Cu–Au system are consistent with DFT data. The melting temperature is predicted within 100 K of the experimental values across the full concentration range. Disordered solid solution to ordered phase transitions exist for all concentrations. Lattice constants deviate by 0.3%–3% from experimental values and the c/a ratio for the $L1_0$

tetrahedral CuAu phase is below unity. Elastic constants are in good agreement with experiment for the pure phases and within a 5%–30% error range for the binary phases.

Acknowledgments

ORCID iDs

Lars Pastewka ⬥ https://orcid.org/0000-0001-8351-7336

References

[1] Gupta R P 1981 *Phys. Rev.* B **23** 6265–70
[2] Finnis M and Sinclair J 1984 *Phil. Mag.* A **50** 45–55
[3] Daw M S and Baskes M I 1984 *Phys. Rev.* B **29** 6443
[4] Ercolessi F, Parrinello M and Tosatti E 1988 *Phil. Mag.* A **58** 213–26
[5] Cleri F and Rosato V 1993 *Phys. Rev.* B **48** 22
[6] Gumbsch P and Daw M S 1991 *Phys. Rev.* B **44** 3934–8
[7] Haberland H, Insepov Z and Moseler M 1995 *Phys. Rev.* B **51** 11061–7
[8] Barrera G D, de Tendler R H and Isoardi E P 2000 *Modelling Simul. Mater. Sci. Eng.* **8** 389
[9] Williams P L, Mishin Y and Hamilton J C 2006 *Modelling Simul. Mater. Sci. Eng.* **14** 817
[10] Borders J 1973 *Thin Solid Films* **19** 359–70
[11] Paulson W M and Hilliard J E 1977 *J. Appl. Phys.* **48** 2117–23
[12] Li Y, Zhu X, Zhang G, Tan J, Wang W and Wu B 2010 *Phil. Mag.* **90** 3049–67
[13] Delogu F and Cocco G 2005 *Phys. Rev.* B **71** 144108
[14] Kaupp G 2009 *CrystEngComm* **11** 388–403
[15] Misra A and Krug H 2001 *Adv. Eng. Mater.* **3** 217–22
[16] Wang J, Hoagland R G, Hirth J P and Misra A 2008 *Acta Mater.* **56** 3109–19
[17] Wang J and Misra A 2011 *Curr. Opin. Solid State Mater. Sci.* **15** 20–8
[18] Zimmerman J A, Gao H and Abraham F F 2000 *Modelling Simul. Mater. Sci. Eng.* **8** 103
[19] Hull D and Bacon D 2011 Dislocations in face-centered cubic metals *Introduction to Dislocations* ed D Hull and D Bacon 5th edn (Oxford: Butterworth-Heinemann) ch 5, pp 85–107
[20] Foiles S M, Baskes M I and Daw M S 1986 *Phys. Rev.* B **33** 7983–91
[21] Zhou X W, Johnson R A and Wadley H N G 2004 *Phys. Rev.* B **69** 144113
[22] Ackland G J and Vitek V 1990 *Phys. Rev.* B **41** 10324–33
[23] Cahn R W 1991 *Adv. Mater.* **3** 628–9
[24] Mishin Y, Mehl M J, Papaconstantopoulos D A, Voter A F and Kress J D 2001 *Phys. Rev.* B **63** 224106
[25] Grochola G, Russo S P and Snook I K 2005 *J. Chem. Phys.* **123** 204719
[26] Tománek D, Aligia A A and Balseiro C A 1985 *Phys. Rev.* B **32** 5051–6
[27] Becker C A, Tavazza F, Trautt Z T and Buarque de Macedo R A 2013 *Curr. Opin. Solid State Mater. Sci.* **17** 277–83
[28] Ercolessi F and Adams J B 1994 *Europhys. Lett.* **26** 583
[29] Martin R M 2004 *Electronic Structure* (Cambridge: Cambridge University Press)

[30] Perdew J P, Chevary J A, Vosko S H, Jackson K A, Pederson M R, Singh D J and Fiolhais C 1992 *Phys. Rev.* B **46** 6671–87

[31] Kittel C 2004 *Introduction to Solid State Physics* 8th edn (New York: Wiley)

[32] Kamran S, Chen K and Chen L 2009 *Phys. Rev.* B **79** 024106

[33] Wang G S, Delczeg-Czirjak E K, Hu Q-M, Kokko K, Johansson B and Vitos L 2013 *J. Phys: Condens. Matter* **25** 085401

[34] Simmons G and Wang H 1971 *Single Crystal Elastic Constants and Calculated Agregates Properties: A Handbook* 2nd edn (Cambridge, MA: MIT Press)

[35] Mattsson A E, Armiento R, Schultz P A and Mattsson T R 2006 *Phys. Rev.* B **73** 195123

[36] Yan J W and Zhang G P 2013 *Appl. Phys. Lett.* **102** 211905

[37] Tyson W and Miller W 1977 *Surf. Sci.* **62** 267–76

[38] Ogata S, Li J and Yip S 2002 *Science* **298** 807–11

[39] Swart J C W, van Helden P and van Steen E 2007 *J. Phys. Chem.* C **111** 4998–5005

[40] Wu X Z, Wang R, Wang S F and Wei Q Y 2010 *Appl. Surf. Sci.* **256** 6345–9

[41] Kresse G and Hafner J 1993 *Phys. Rev.* B **47** 558

[42] Kresse G and Furthmüller J 1996 *Comput. Mat. Sci.* **6** 15

[43] Kresse G and Furthmüller J 1996 *Phys. Rev.* B **54** 11169

[44] Blöchl P E 1994 *Phys. Rev.* B **50** 17953

[45] Perdew J P, Burke K and Ernzerhof M 1996 *Phys. Rev. Lett.* **77** 3865–8

[46] Monkhorst H J and Pack J D 1976 *Phys. Rev.* B **13** 5188–92

[47] Methfessel M and Paxton A T 1989 *Phys. Rev.* B **40** 3616–21

[48] Vítek V 1968 *Phil. Mag.* **18** 773–86

[49] Reed R 2008 *The Superalloys: Fundamentals and Applications* (Cambridge: Cambridge University Press)

[50] Paidar V and Vitek V 2002 *Stacking-Fault-Type Interfaces and Their Role in Deformation* (New York: Wiley) pp 437–67

[51] Yan Z, Perdew J P and Kurth S 2000 *Phys. Rev.* B **61** 16430–9

[52] Pitarke J M and Eguiluz A G 2001 *Phys. Rev.* B **63** 045116

[53] Skilling J 2004 *AIP Conf. Proc.* **735** 395–405

[54] Skilling J 2006 *Bayesian Anal.* **1** 833–59

[55] Pártay L B, Bartók A P and Gábor C 2010 *J. Phys. Chem.* B **114** 10502–12

[56] Pártay L B, Bartók A P and Gábor C 2014 *Phys. Rev.* E **89** 022302

[57] Baldock R J N, Pártay L B, Bartók A P, Payne M C and Csányi G 2016 *Phys. Rev.* B **93** 174108

[58] Burkoff N S, Baldock R J N, Várnai C, Wild D L and Csányi G 2016 *Comput. Phys. Commun.* **201** 8–18

[59] Foiles S, Baskes M and Daw M 1986 *Phys. Rev.* B **33** 7983

[60] Tersoff J 1988 *Phys. Rev.* B **37** 6991

[61] Nelder J A and Mead R 1965 *Comput. J.* **7** 308

[62] Ozoliņš V, Wolverton C and Zunger A 1998 *Phys. Rev.* B **57** 6427–43

[63] Paxton A T 1992 Point, line and planar defects *Electron Theory in Alloy Design* ed D G Pettifor and A H Cottrell (London: The Institute of Materials) pp 158–90

[64] Rosengaard N M and Skriver H L 1994 *Phys. Rev.* B **50** 4848–58

[65] Paxton A T and Sun Y Q 1998 *Phil. Mag.* A **78** 85–104

[66] Xie H, Yu T and Yin F 2014 *Mater. Sci. Eng.* A **604** 142–7

[67] Okamoto H, Chakrabarti D, Laughlin D and Massalski T 1990 *Au–Cu (Gold-Copper), Binary Alloy Phase Diagrams* vol 1 ed T B Massalski 2nd edn (Materials Park, OH: ASM International)

[68] Honeycutt J D and Andersen H C 1987 *J. Phys. Chem.* **91** 4950–63

[69] Stukowski A 2012 *Modelling Simul. Mater. Sci. Eng.* **20** 045021

[70] Larsen P M, Schmidt S and Schiøtz J 2016 *Modelling Simul. Mater. Sci. Eng.* **24** 055007

[71] Perdew J P, Ruzsinszky A, Csonka G I, Vydrov O A, Scuseria G E, Constantin L A, Zhou X and Burke K 2008 *Phys. Rev. Lett.* **100** 136406

[72] Plimpton S 1995 *J. Comput. Phys.* **117** 1–19

[73] Larsen A *et al* 2017 *J. Phys.: Condens. Matter* **29** 273002

[74] http://github.com/libAtoms/matscipy

[75] http://github.com/libAtoms/pymatnest

[76] Stukowski A 2010 *Modelling Simul. Mater. Sci. Eng.* **18** 15012